



An Automatic Model Combining Descriptors of Gray-Level Co-Occurrence Matrix and HMAX Model for Adaptive Detection of Liver Disease in CT Images

Sanaz Bagheri¹, Somayeh Saraf Esmaili^{2*}

¹Department of Biomedical Engineering, South Tehran Branch, Islamic Azad University, Tehran, Iran.

²Department of Biomedical Engineering, Garmsar Branch, Islamic Azad University, Garmsar, Iran.

Received: 6-Nov-2018, Revised: 15-Dec-2018, Accepted: 17-Dec-2018.

Abstract

Liver cancer emerges as a mass in the right upper of the abdomen with general symptoms such as jaundice and weakness. In recent years, the liver cancer has been responsible for increasing the rate of deaths. Due to some discrepancies in the analytical results of CT images and the disagreement among specialists about different parts of the liver, accurate diagnosis of possible conditions requires skill, experience, and precision. In this paper, a new integrative model based on image processing techniques and machine learning is provided, which is used for segmentation of damages caused by the liver disease on CT images. The implementation process consists of three steps: (1) using discrete wavelet transform to remove noise and separate the region of interest (ROI) in the image; (2) creating the recognition pattern based on feature extraction by Gray-Level Co-occurrence matrix and hierarchical visual HMAX model; reducing the feature dimensions is also optimized by principle component analysis and support vector machine (SVM) classification, and finally (3) evaluating the algorithm performance by using K-fold method. The results of implementation were satisfactory both in performance evaluation and use of features selection. The mean recognition accuracy on test images was 91.7%. The implementation was in the presence of both descriptors irrespective of feature dimension reduction; with unique HMAX model and feature dimension reduction and application of both descriptors and reduction of feature dimensions and their effect on recognition were measured.

Keywords: Liver CT scan, gray-level Co-occurrence matrix, hierarchical visual HMAX model, support vector machine.

1. INTRODUCTION

Liver-related diseases and liver cancers are

one of the leading causes of death in the world [1-4]. Liver cancer is the growth of liver cancer cells that emerge as a mass in the right upper abdomen with general

*Corresponding Author's Email: s.sesmaeily@iau.garmsar.ac.ir

symptoms such as jaundice and weakness [6]. In recent years, there has been an increase in cases caused by this disease [7]. A variety of factors such as hepatitis C, chronic hepatitis, cirrhosis, fungal toxin aflatoxin, obesity, hemochromatosis, excessive consumption of alcohol and Trisomy 18 can be the underlying cause of liver disease [5]. Sometimes it is both complicated and difficult to diagnose these irregularities in liver. There are several ways for the liver diagnosis, including:

- 1 -Liver (Hepatocellular) cancer screening and Alpha-fetoprotein tests every 6 to 12 months
2. If cancer is suspected, further tests are conducted to determine the stage of the disease with sampling
3. Imaging using MRI and CT-scan

In the first technique, i.e. diagnosis at the primary level, error probability was low, but it was invasive and time consuming. In the second technique, i.e. testing repeatedly, it was contingent upon the completion of the first step and the third technique illustrated various sections of tissue based on liver imaging [8, 9]. The classification of liver tumors is of critical importance before any surgery. It also plays a crucial role in the development of 3D tumor surgery. This can help surgeons to remove the entire tumor. The accurate and primary diagnosis of the tumor is crucial to the treatment of the disease. Given discrepancies in the results of CT images and disagreements among doctors regarding different parts of the liver, the accurate diagnosis of possible conditions require skill, experience and precision, and in some cases, even skilled specialists may come up with diverse results. According to the literature on CT images, in 2 to 5 out of 10 cases, interpretation could be erroneous. This is also true for liver images [10]. Therefore, intelligent diagnosis of liver

cancer in CT images can largely contribute to more accurate decisions of specialists.

This paper deals with the diagnosis of liver disease and cancer using automated methods based on the analysis of CT images. The primary goal of proposing and designing such a method is the implementation of an intelligent system based on machine learning, which is able to determine the presence or absence of disease by relying on statistical learning techniques, and then based on the features extracted from the liver region, the classification is provided. The following assumptions are considered in this system:

1. The system consists of sub-algorithms including CT image processing, feature extraction and classification of various image parts that are characteristic of cancer and can finally provide an integrated performance.
2. The accuracy, sensitivity and specificity of the proposed method would be higher than previous techniques.

The paper is organized as follows: in the Section 2, we have literatures review. Section discusses the proposed method, which combines feature extraction structure of CT images, processing method and support vector machine (SVM) classification. Practical results and findings are discussed in Section 4 and finally conclusions are drawn in Section 5.

2. LITERATURES REVIEW

In recent years, the analysis of CT images of different organs, including liver has attracted growing attention of researchers. Nonetheless, there seems to be a discrepancy among researchers with regard to the algorithm design. Lee et al. [11] carried out the classification process using fractal-based feature extraction method underpinned by M-band wavelet transforms.

However, they did this for ultrasonic images, which were classified on the basis of healthy liver, cirrhosis and hepatoma.

In the same year, Gletsos et al. [12] proposed a diagnostic system that used neural network classifier for the detection of liver lesions in CT images. The region of interest (ROI) was made of normal tissue, liver cysts, hemangioma and hepatocellular carcinoma in CT images.

In 2006, Lim et al. [13] discussed the difficulty of constructing a 3D model of the liver and the extraction of features from CT images, they suggested the direct separation of areas suspected of the disease.

Mougiakakou et al. [14] proposed differential diagnosis for lesions concentrated in the recipient area of the liver on CT images using texture features, feature selection and ensemble driven classifiers.

Okada et al. [15] suggested automatic segmentation of the liver to create a diagnostic model using probabilistic atlas and multi-level statistical shape model.

In a detailed study by Heimann et al. [16], they compared and assessed different methods of separating different parts of liver tissues. They tested models such as statistical shape models, atlas registration active contour, cut graphs and rule-based systems.

Automatic isolation and detection of liver lesions in CT images with optimized automatic was presented by Militzer et al. [17]. Their strategy involved using a probabilistic boosting-tree to classify points or regions suspected of glands and tissue lesions.

The restoration of CT images of liver lesions based on the degree of similarity was proposed by Napal et al. [18]. They utilized 30 samples of CT images and explored a total of three classes of healthy tissue, hemangioma and metastasis.

Selver et al. [19] attempted to assess and use unsupervised techniques such as K-means or neural network to separate masses suspected of tissue lesions in the liver and CT images.

The application of Weka method as an efficient algorithm for segmentation and classification of CT images was presented by Quatrehomme et al. [20] with the goal of separating concentrated lesions in the liver and their evaluation for 5 classes. Co-occurrence matrix, morphological features and tissue features were extracted and an accuracy of 74% was obtained for different sizes of lesion tissues in CT images of these 5 classes.

Zaidan et al. [21] used a combination of techniques such as active contour, watershed-based separation and neural networks in CT images and reported an accuracy of 92%. Also, a classification accuracy of 90% was achieved in tumors or lesions.

Similarly, Li et al. [22] used active contour and semi-automatic separation in CT images, but they found little discrepancy in input CT images of the sample liver.

Casciara et al. [23] performed automatic separation of liver tissue and hepatic-induced tumors through a three-dimensional model of CT images. In this study, two solutions were presented and the results were compared.

Gnnasundari et al. [24], using histogram analysis and morphological filtering, suggested initial clustering of images followed by segmentation of different parts and then feature extraction. Xu et al. [25] employed restoration of CT images, conceptual shape and texture descriptors, and reported 90% to 100% accuracy.

Virmani et al. [26] used main operational analysis and support vector machines to separate tissue lesions from ultrasound images and reported an accuracy of 85% to

95%. Ji et al. [27] combined multiple atlases optimized moderate transmission separation in an attempt to separate and classify different parts of the liver tissue.

Automatic separation of liver lesions was studied by Kumar et al. [28]. They considered it as a critical step in the diagnosis of diseases related to liver. Therefore, they adopted fuzzy clustering and comparison with manual methods for this purpose.

Ozturk et al. [29] used ripplelet transform of Curvelet transform and artificial neural networks via the analysis of MRI images. They demonstrated the presence or absence of disease. Balagurunathan et al. [30] used CT image analysis of different areas including liver. Their method indicated the possibility of separating important features that could be incorporated for the diagnosis and prognosis of possible diseases in liver organs.

Singh et al. [31] proposed information fusion and feature extraction of ultrasonic images, which separated masses suspicious for cancer and hazardous lesions and reported 95% accuracy.

Tomoshige et al. [32] proposed the statistical shape model together with error estimation, which was primarily used for separating different parts of the liver and CT images with low contrast. They also exploited pipeline and graph cut techniques for segmentation.

Another semi-automatic separation method used for determining and separating tumors and other tissues in CT and PET images was proposed by Hirata et al. [33]. Mala et al. [34] suggested the tissue analysis of CT images based on neural network for classifying Cirrhosis tissue and fat. For this purpose, they presented probabilistic neural network that was used in combination with linear vector quantization neural networks.

In addition to CT images of liver, some researchers have attempted to separate tissues such as pancreas and stomach including Roth et al. [35]. They applied deep neural network (DNN), frequent clustering technique and environmental mold to CT images for separation and calculation of accuracy.

Conze et al. [36] used stratified random separation and super-voxels for CT images, which allowed the separation of liver tumors in a semi-automatic fashion. Therefore, they utilized a convolution mask of CT images and separated three-dimensional mold from other parts.

Similar to studies on separation, Mustafa et al. [37] proposed a method with an accuracy of 91.3% for separating different parts of the liver in CT images, which allowed segmentation in case of liver tumor or lesion.

3. THE PROPOSED METHOD

As mentioned above, the algorithm proposed in this paper is capable of learning and being used in hospitals and clinics specialized in liver diseases. The implementation steps of the proposed method are shown in Fig. 1.

3.1. Database

The main data comprised of images of all types for patients with different levels of liver disease, lesion or cancer, which had been gathered over a two year period (2014 to 2017) from Sabzevar hospitals in Khorasan Rezavi Province, Iran.

In addition to healthy subjects, the patients were divided into two groups with and without history of pain in the liver, and the different CT scan imaging centers reporting various images. The imaging machine was a Siemens CT scan device (SOMATOM Emotion 16) with the lowest

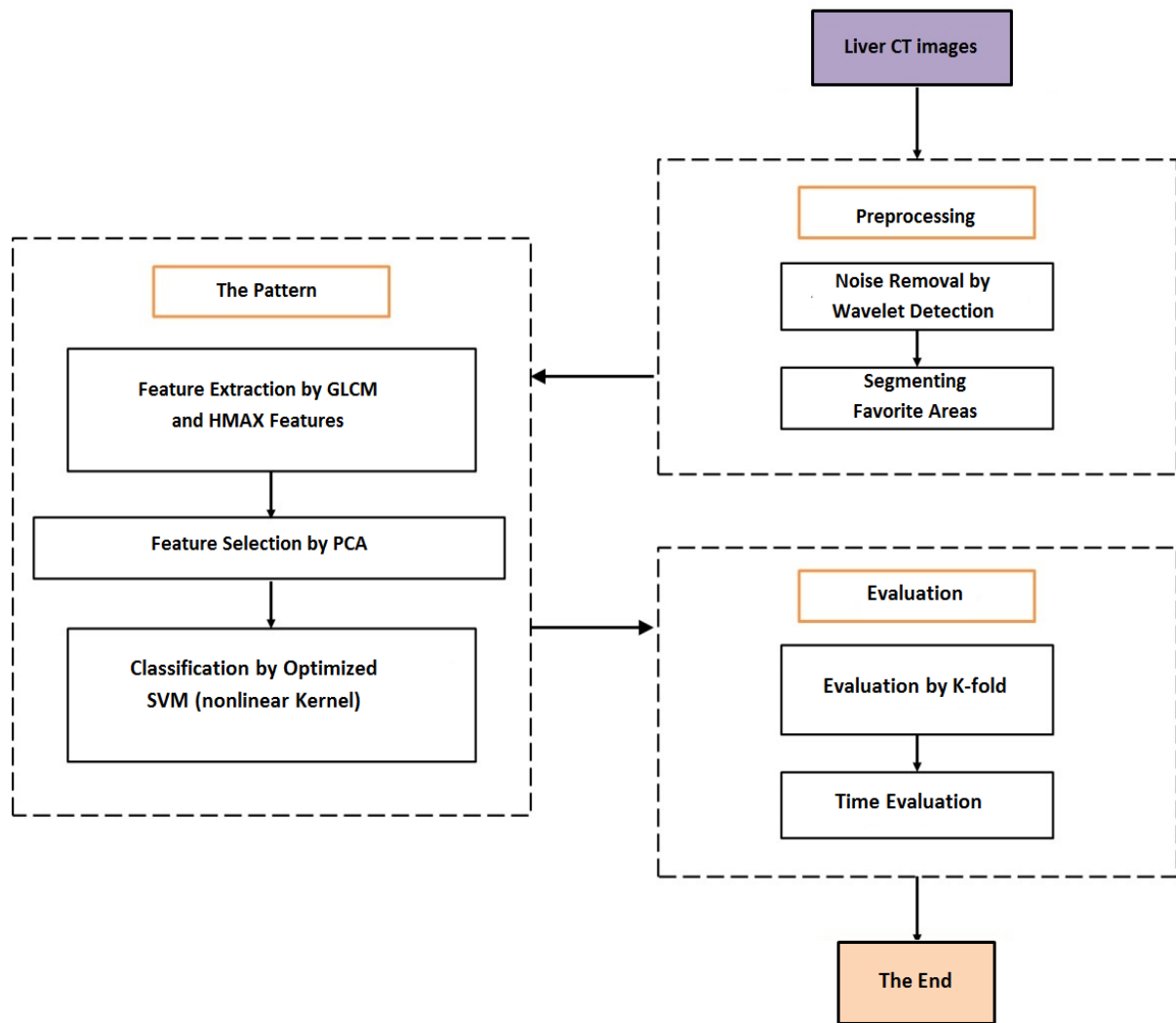


Fig. 1. Flowchart of the proposed method for determining liver disease.

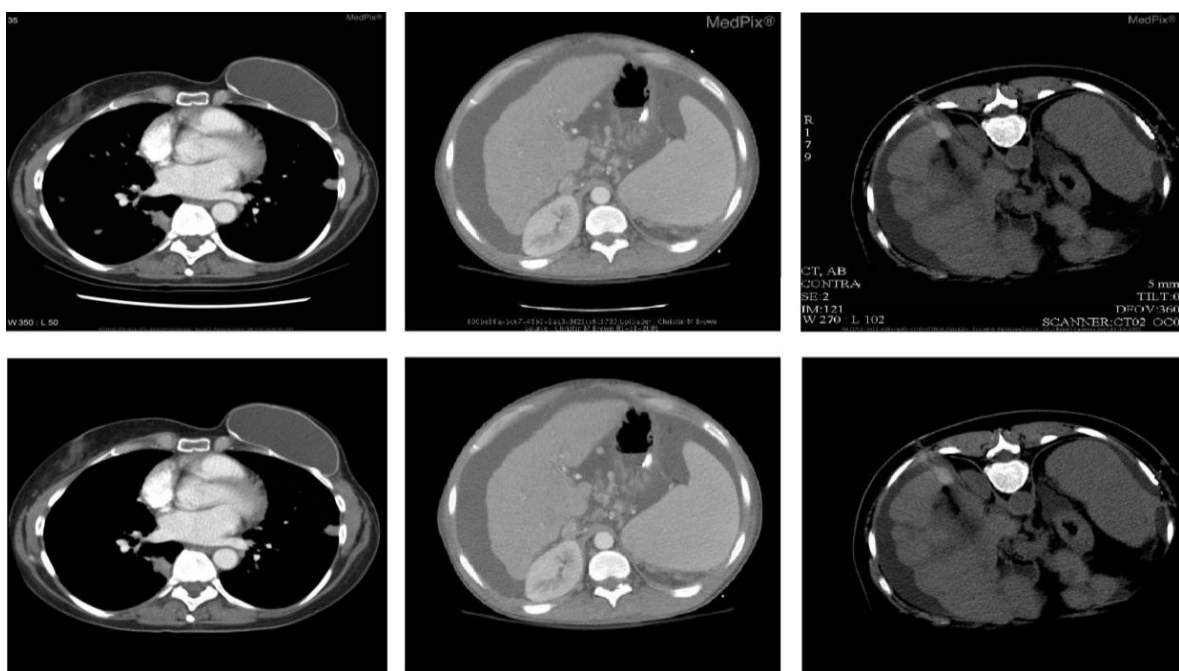


Fig.2. Sample input images (first row) and pre-processed images (second row).

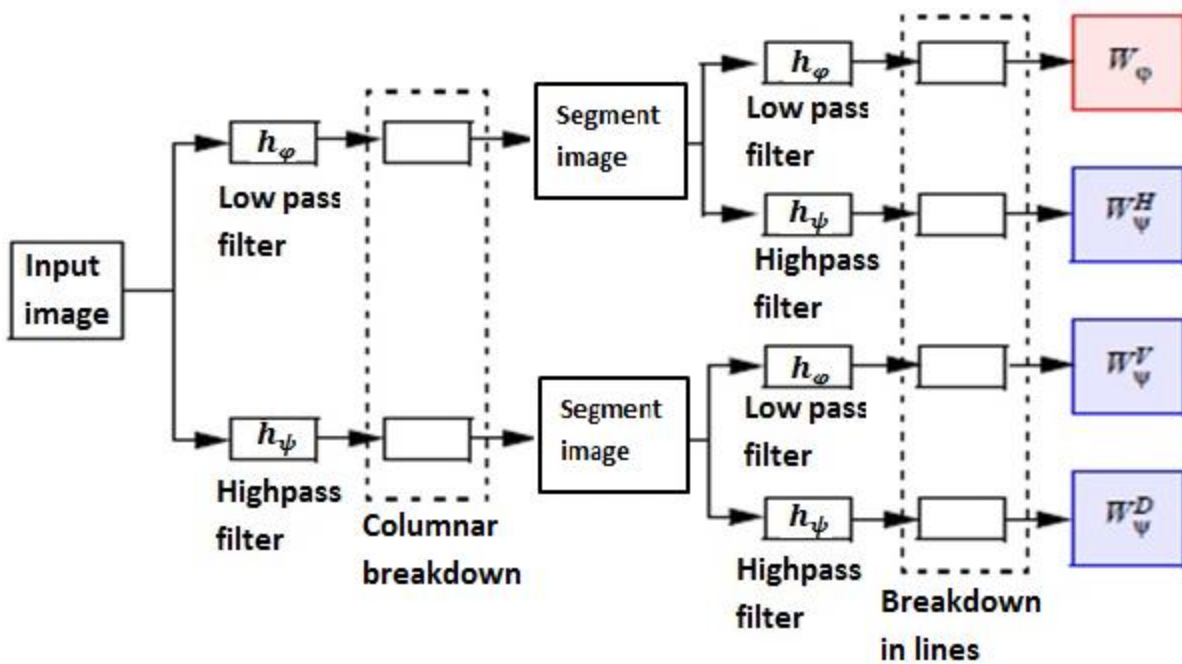


Fig. 3. Two-dimensional discrete wavelet transform in four directions for a sample input of CT images.

radiation dose and reduced radiation such as IRIS, CARE Dose 4 D, and Dose MAP.

The paper involved gathering data of a cross-sectional study on two groups of subjects. The sample consisted of 135 subjects who were diagnosed by a physician and radiologist in the CT scan Imaging Center of hospital, who were divided into two test ($n= 59$) and control ($n= 76$) groups. In fact, 59 subjects were assigned to the group of patients with liver disease and 76 healthy subjects that showed no side effects of the disease were assigned to the control group. Two specialists gave their definitive diagnosis about the disease and in some case the possible location of the lesion.

3.2. Preprocessing

3.2.1. Region of Interest (ROI)

The mechanism of separating regions of interest in the image is not straightforward, and the tissue may be damaged in a way that prohibits the application of conventional separation methods.

However, by changing the contrast of the image or brightness intensity of pixels, separation can be made in some specific points to isolate the ROI from other parts. In the sample CT image P , background and foreground regions are separated from each other. By doing so, we seek to construct the optimized background and find the best neighborhood. Pixel neighborhood refers to the pixels adjacent to pixels under study, which is depicted by coordinates (x, y) , as shown by Eq.(1):

$$P_{i,j} : (i \pm 1, j), (i, j \pm 1) \quad (1)$$

As a result, none of neighborhoods (i, j) will exceed the value of 8 neighborhoods, unless the neighborhood set is extended. The pixel movement can be started from a pixel $P(i, j)$ and spreads in different directions. The same rule applies to the removal of unimportant parts. The selection of quadruple proximity has often a favorable effect on selecting ROI in the liver image. An example of pre-processed images is

shown in Fig. 2. However, it should be noted that the selection of a very high neighborhood also leads to the elimination of more elements, and a compromise must be made for this purpose. Usually choosing the 4th proximity will have a more favorable effect in choosing the area of interest in the liver image.

3.2.2. Noise Removal

By applying a one-dimensional discrete wavelet transform to each row, assuming that columns are constant, corresponding signals are achieved, and then this process, assuming that rows are constant, is again applied to all columns and therefore rows of rate 2 are sampled [38, 39].

If an image is decomposed into n levels of basic functions, the first level will consist of high-frequency and the n th level will contain low-frequency components.

Discrete wavelet transform coefficients, which are also decomposed in fitting with the frequency ranges of each basic function, contain local information of the original image [40-42]. After two-dimensional discrete wavelet transform implementation, it is sufficient to build coefficients S_j at the level 1. Thus, S_j is in fact a classification of the original image and its constructing coefficients, they are an estimate of different brightness intensities, or pixel categories in a neighborhood that are identical in terms of lighting intensity. After applying this transform to the image, four image levels are achieved according to the frequency of samples. In Fig. 3, two-dimensional discrete wavelet transform in four directions are shown for a sample input of CT images. Several samples of the signal corresponding to several rows and columns from a liver CT are shown in Fig. 4.

3.3. Feature Extraction

3.3.1. Gray-Level Co-occurrence Matrix Features (GLCM Features)

In the process of feature extraction, the objective is to find mapping in the solution space, which is able to reduce the dimension of patterns for the classification stage. For this purpose, two feature extraction techniques are used and then the final vector features with aggregate output of the two descriptors is achieved. In the statistical methods, spatial distribution of gray levels in tissue is the basis of classification by calculating the local features in each point of the image and extraction of a set of statistics. Some examples of these methods are GLCM-based [43] methods and gray-level difference techniques [44]. The signal processing techniques based on frequency content include wavelet-based analysis [45], Gabor transform [46] and Curvelet transform [47]. GLCM is a square matrix whose elements indicate the relative frequency of occurrence for a pair of gray values at a specific distance in the same direction. The elements of a co-occurrence matrix of $G \times G$ dimension for a distance vector of d ($dx = dy$) are defined according to Eq. (2):

$$P_d(i, j) = \{((r, s), (t, v)) : I(r, s) = i, I(t, v) = j\} \quad (2)$$

where $I(.,.)$ shows an image of $N \times N$ dimension and G levels of gray. The co-occurrence matrix in fact describes frequencies related to P_{ij} where two separate neighboring pixels at a fixed distance d , one with the grey intensity of i and the other with the grey intensity of j , take place in the image.

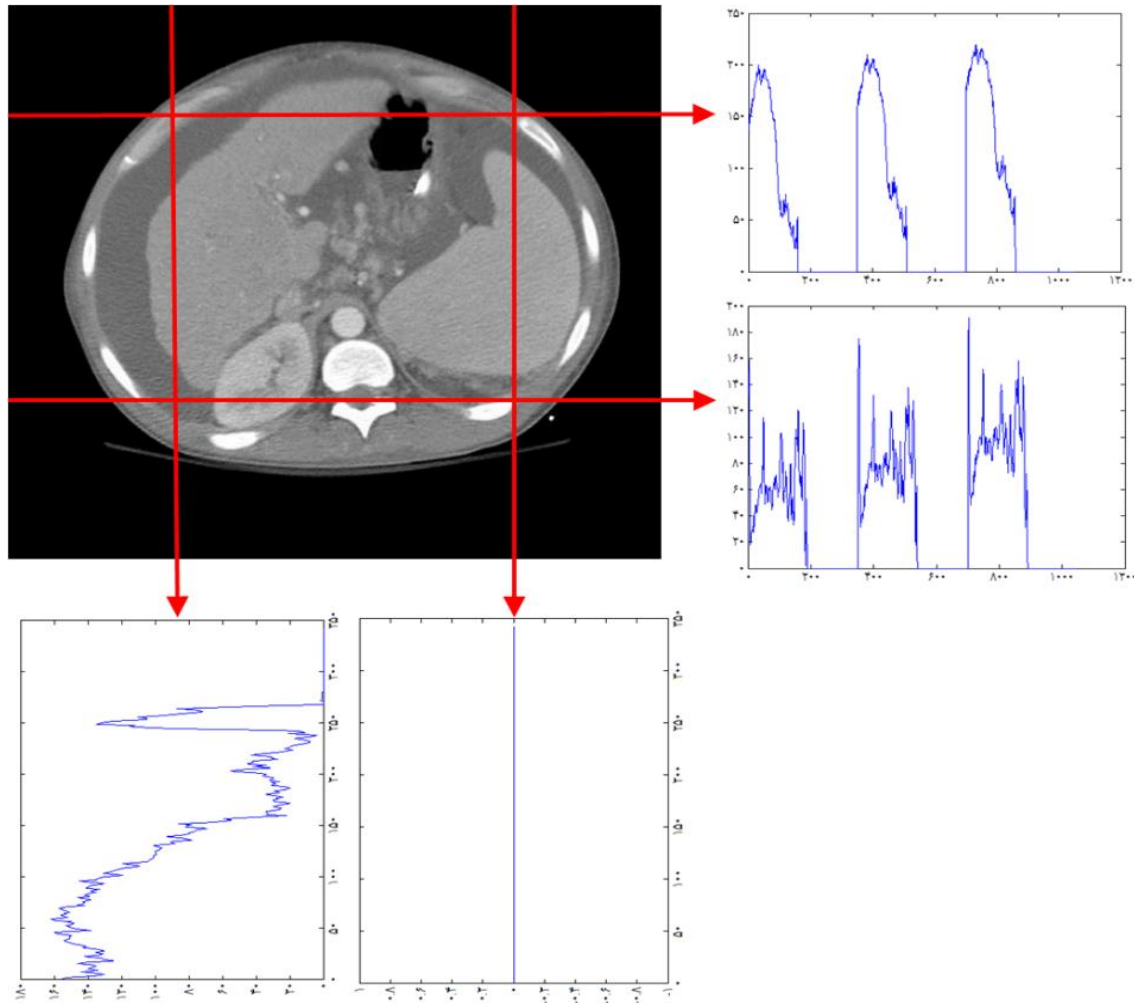


Fig. 4. Represents multiple signal samples corresponding to several rows and columns from a CT image of a liver in two-dimensional discrete wavelet transformation.

Then, the co-occurrence matrix is made of a square matrix whose size depends on the maximum intensity of the gray pixels in the image. Each element P_{ij} indicates the frequency of events for the above structure: a pixel of size i at the fixed distance of d from a pixel of size j . If the distance is $d = 1$, then four directions are perceivable and the angles between two pixels could be expressed as 0, 45, 90 or 135 degrees.

In other words, in this method, the image is converted into a two-dimensional matrix where each item indicates the possibility of color intensity I and j being juxtaposed at a neighboring distance d and angle θ . Finally, using functions defined based on this matrix, features are extracted.

3.3.2. Hierarchical Visual HMAX Model Features

The hierarchy analysis technique was first proposed by Hubel and Wiesel where the visual cortex of a cat's brain and then a monkey's brain were being studied [48, 49]. The S1 units of the input image are decomposed into simple S1 units through a multi-dimensional array where these simple units are formed based on simple and classic V1 cells. These units are formed in accordance with a basic mode of simple cells. In other words, they consist of a row of unidirectional filters and alternative on and off areas that share a common axis that defines the cell direction. The population of

S1 units includes 136 types of units, i.e. 2 modes in 4 directions and 17 sizes, but in this model, the 64-model was adopted. Fig. 5 depicts different weight vectors that correspond to various units.

Similar to other simple units in the model, S1 units carry out the adjustment operation for incoming algorithms from input x and weight vector w .

When x corresponds to w , the response of a S1 unit is maximal. In mathematical terms, the weight vector w associated with S1 units takes the form of a Gabor function, which is a suitable model for recipient strings of simple cells and can be described by Eqs. (3) and (4):

$$F(x, y) = \exp\left(-\frac{(X^2 + \gamma^2 Y^2)}{2\sigma^2}\right) \times \cos\left(\frac{2\pi}{\lambda} X\right) \quad (3)$$

$$\begin{cases} x_0 = x \cos \theta + \gamma \sin \theta \\ y_0 = -x \sin \theta + \gamma \cos \theta \end{cases} \quad (4)$$

All filter parameters, i.e. the size of function in space or γ , angle or θ , effective bandwidth or σ and wavelength λ are adjusted to match the biological type. S1 filters are arranged as a pyramid of different scales (in degrees) in the range of 7×7 to 37×37 pixels sizes. To limit the number of units, four directions were considered, which included 0, 45, 90 and 135 degrees. Finally, a total of 64 different recipient fields of S1 (i.e. 16 degrees in four different directions) were obtained.

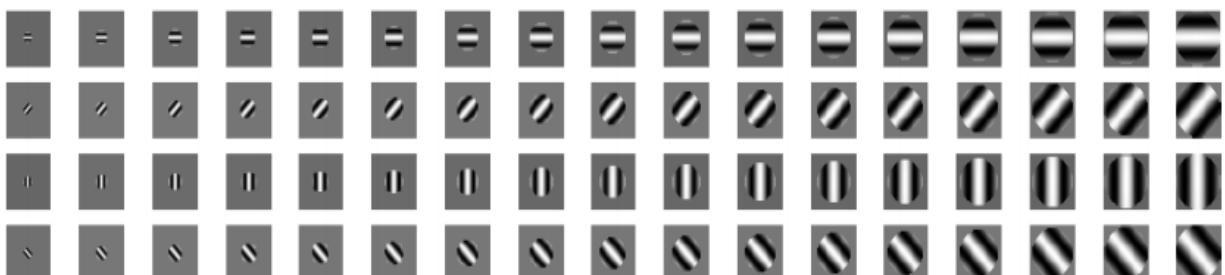


Fig. 5. The reception field of simple S1 (derived from Gabor filter) [50].

The next layer or C1 corresponds to complex cells in the visual cortex of the brain. Each complex C1 receives aggregate outputs from simple S1 units of the first layer in the same direction (and in two reverse modes) but in slightly different positions and sizes. Operations that are integrated with responses of S1 units in the layer C1 are called MAX linear actuator. The response of C1 unit is determined by the strongest input.

Considering the integration of S1 units in slightly different positions but with identical direction, the corresponding C1 units are rendered insensitive relative to the stimulating positions within its recipient field. As a result of integrating S1 units of narrow differences, large areas of broadband for S1 and C1 units are created, which correspond to the biological type.

C1 units are integrated on the output of organized S1 units derived from the previous layer in the same direction and scale bands with each band scale consisting of 2 filter sizes. There are 8 scale bands for the entire sizes of S1 filter. For example, the band scale contains S1 filters of 7×7 and 9×9 sizes. The process is implemented for all of the four directions and each band separately. The integration shores up resistance against two-dimensional changes from S1 to C1 layers. The corresponding integration process will be a MAX operation.

In S2 layer or level, different activities of complex layers are integrated on a small neighborhood in different directions (It should be noted that the neighborhood size determines the size of the recipient unit of S2 unit). Computations that are integrated over these time periods constitute the adjustment operation. As a result, from C1 to S2 units, both the selectivity of units and complexity of stimuli are reinforced. Thus, at the level C1, units are selected for a single rod in a particular direction, while in S2 level, units are selected for complex patterns such as integration of directional rods to create the edge or select a border.

3.4. Dimension Reduction

Principal component analysis is an unsupervised method derived from linear transform that map input data on a special atmosphere. Assuming that M training samples are available, the matrix of visual data based on $X = x_1, x_2, \dots, x_m$ is formed. The transposed version of this matrix is Y where $Y = X^T$. The data center in visual space is obtained using the mean vector $m = \frac{1}{M} \sum_{j=1}^m X_j$. Then, by subtracting the mean vector m from each training vector, which is displayed as $x_j = (x_j - m)$, the matrix of column data based on $x_c = \bar{x}_1, \bar{x}_2, \dots, \bar{x}_m$ is formed, which is called the control vector. Covariance matrix of data set is obtained as,

$$Cov_x = \frac{1}{M} \sum_{j=1}^m \bar{x}_j \bar{x}_j^T = \frac{1}{M} x_c x_c^T \quad (5)$$

By measuring the diameter of Cov_x , principal components are obtained. These are components of orthogonal image on eigenvectors obtained by resolving the eigenvalue equation.

$$P^T Cov_x P = \Pi \quad (6)$$

where Π and P are diagonal matrix of eigenvalues and orthogonal matrix of eigenvalues. Geometrically, p is a rotational matrix that rotates the main coordinate system based on eigenvectors so that the eigenvalue vector correlates with the maximum vector value. In this case, it is called maximum variance axis.

Only eigenvalues β do correlate with the largest eigenvalues, which are then utilized to define the subspace where β is the expected size of the space.

There are three factors to adapt the image with the subspace of eigenvector β . Hence, dimension reduction is used as a way of scaling back computations. Fig. 6 displays transfer from space coordinates to the new coordinate. The first axis should be in a direction that maximizes data variance. In other words, axis is oriented in the direction with the greatest data dispersion. The second axis should be perpendicular to the first axis, in a way that data variance is maximized. In the process of implementing the algorithm.

3.5. Classification by Support Vector Machine (SVM)

SVM is an optimal separation method, the output of which is obtained using Bisian theory [50, 51]. Where the estimation model is not widely available in terms of data size, SVM is used. The solution maps the non-detachable data to another, and looks for a cloud with the largest margin for data breakdowns. Assuming that the training data of the preceding stage, using the weight assigned, has a special label and is represented as $S = (x_i, y_i)$, in the sense that $i = 1, \dots, l$, and $Y_i = \{-1, 1\}$, then the backup vector machine forms experimental x data using the learning of nonlinear functions as,

$$f(x) = \text{sgn}\left(\sum_{i=1}^l \alpha_i y_i K(x_i, x) + b\right) \quad (7)$$

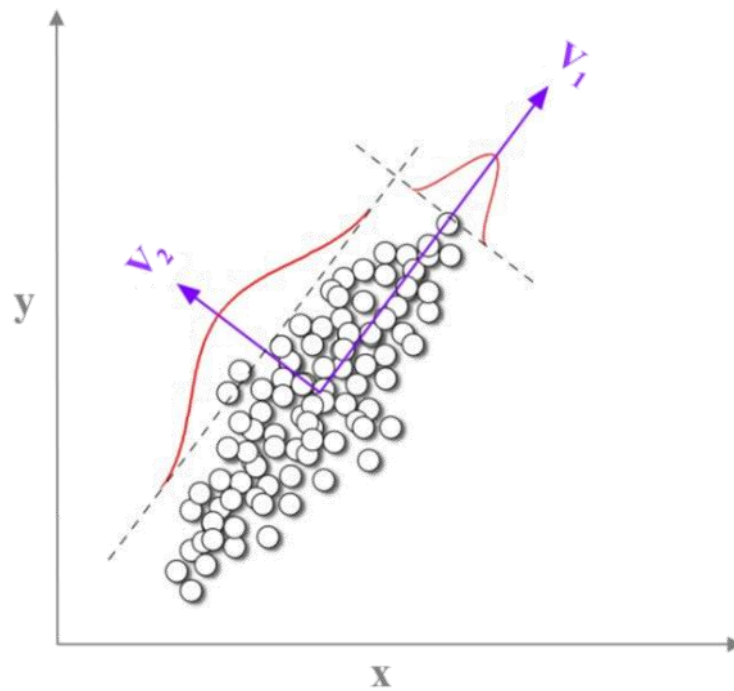


Fig. 6. Transfer from the first coordinate system to the second coordinate space.

in which the Lagrange multiplication α_i is a dual optimization problem that describes the cloud. Also, $K(x_i, x_j)$ is the kernel function, which is expressed,

$$\phi(x_i)^T \phi(x_j) \quad (8)$$

where ϕ is a nonlinear function mapping data into a wider space. On the other hand, b is the optimum super-plane threshold parameter. Educational data x_i with $\alpha_i > 0$ is read support vectors, and the SVM finds a super-plane, that in which the distance between the support vectors and the super-plane is maximized. Linear polynomials and radial base function kernels are most used in the kernels of this class. In a kernel function instead of multiplying the point, the converted vectors are replaced, and the clear form of the convergent function (x) , Φ is not necessarily known. In addition, the use of the kernel function strongly requires less computing. The formulation of the kernel function is based on the point multiplication of a particular case from the viewer's theory.

The problem of optimization is written as,

$$\sum_{i=1}^k \alpha_i - \frac{1}{2} \sum_{i=1}^k \sum_{j=1}^k \alpha_i \alpha_j y_i y_j K(x_i, x_j) \quad (9)$$

This equation must be maximized, and on the other hand, the condition of Eq. (9) must also be true:

$$\sum_{i=1}^k \alpha_i y_i = 0 \text{ and } 0 \leq \alpha_i \leq C \quad (10)$$

for $i = 1, \dots, k$

Therefore, the decision function is represented as Eq. (11):

$$f(x) = \text{sign} \left(\sum_{\text{Support Vector}} y_i \alpha_i^o K(x_i, x) + b^o \right) \quad (11)$$

The best kernel function for solving classification problems is the radial basis function,

$$\exp \left(\frac{-\lambda \|x - x_i\|^2}{2\sigma} \right) \quad (12)$$

4. IMPLEMENTATION AND EVALUATION OF THE PROPOSED ALGORITHM

The evaluation is done in two steps, the first step being to evaluate the performance of the method with a large amount of features, and the second step will include few features. In both steps, the sensitivity, accuracy and accuracy of the K-fold are measured.

4.1. Preprocessing

After decontamination and improving the contrast of liver CT images, a percentage of degradation is associated with the available data, which is negligible. However, in order to assess the proposed strategy for eliminating possible noise and improving detail, two criteria are used. The first is mean square error (MSE) and the second is peak signal to noise ratio (PSNR).

$$MSE = \frac{1}{mn} \sum_{i=0}^{m-1} \sum_{j=0}^{n-1} [I(i, j) - K(i, j)]^2 \quad (13)$$

where I is the main image of the input CT and K is the image restored after the noise is removed and the details are reinforced. This is the difference between the predicted value of the model or the statistical estimator and the actual value. In fact, RMSD is a good tool for comparing prediction errors with a dataset, discussing differences in pixel values and their variations, and it is not applicable for comparing multiple datasets. They also call these distinct differences, and the average square root error is used to collect them in a number. By comparing peer-to-peer pixels in the main image of the liver (I) and the reconstructed, noise can be cut off to the limit. The resulting error is calculated as the second power and is divided into image dimensions.

PSNR is often used to measure the quality of an image at the time of

compression and image expansion:

$$PSNR = 20 \log \left[\frac{255}{\text{Sqrt}(MSE)} \right] \quad (14)$$

The Suitable values of calculated PSNR after each mode changing are in the range of 20dB to 50dB. Preprocessing benchmarks were performed for different hepatotoxic images of different sizes. The groups were divided into 8 groups and the preprocessing stages were performed on them. The first five groups contain 16 images and the last three groups contain 15 images. Benchmark noise reduction parameters and enhancement details for liver CT images based on categorization in 8 random groups and different image dimensions are shown in Table 1.

The MSEs and PSNRs in Table 1 have suitable values which indicate the proper performance of preprocessing in noise elimination.

4.2. Feature Extraction

HMAX-derived vectors, also known as C2-derived vectors, were introduced by the HMAX model and the model explained in part 3-3-2. These features are extracted from the liver CT images. The image is grayed out and on the S1 layer, Gabor filters is applied in 4 directions. In the C1 layer, the units of the S1 layer reach the maximum value for invertebrate state and local scale. On layer S2, units are extracted as a comparative processing template of the form C1. Only one aspect of importance is taken to optimize the space between the S2 and its input. The C2 layer has units that process the extraction process of S2 units in the entire image. In this layer, spatial and scale information is removed to omit the unstructured position and scale. In Fig. 7, a sample image with contour region is displayed for extracting the HMAX features [50].

Table 1. Benchmark noise reduction parameters and enhancement details for liver CT images based on categorization in 8 random groups and different image dimensions.

Final average	average	Group8	Group7	Group6	Group5	Group4	Group3	Group2	Group1	Image dimensions	Benchmark noise reduction parameters
20.18	5.19	2.67	6.12	9.37	3.54	3.92	3.04	5.02	7.79	32×32	MSE
	8.83	7.11	7.82	4.74	11.32	8.31	14.69	9.77	6.95	64×64	
	16.58	15.92	31.33	9.79	24.77	7.92	16.25	11.24	15.45	128×128	
	50.14	55.72	58.08	32.67	122.48	36.9	24.89	38.64	31.77	256×256	
36.97	41.36	43.86	40.26	38.41	42.63	42.19	43.29	41.12	39.16	32×32	PSNR
	38.88	39.61	39.15	41.37	37.59	38.93	36.46	38.23	39.71	64×64	
	36.33	36.11	33.17	38.22	34.19	39.14	36.02	37.62	36.24	128×128	
	31.32	30.67	30.49	30.16	27.25	32.46	34.17	32.26	33.11	256×256	

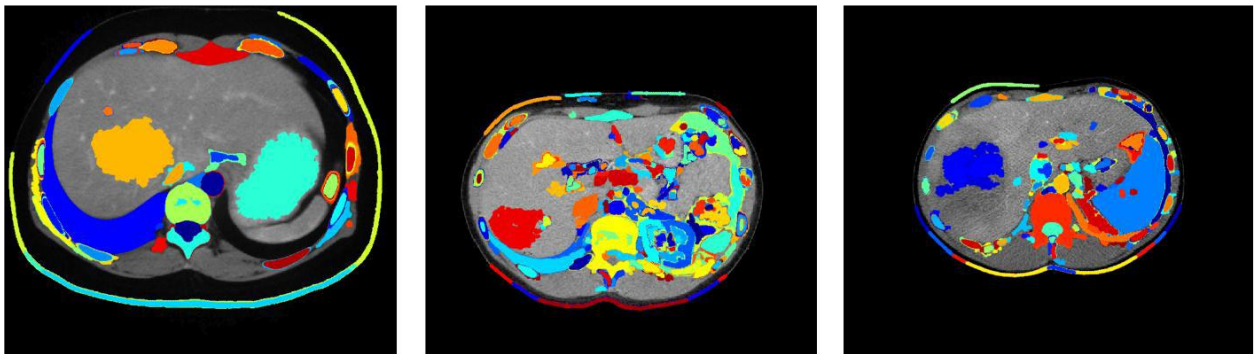


Fig. 7. A sample of integrating contour areas by HMAX features.

Since rotation of image leads to the transfer of coefficient between sub-bands of a scale, to establish independence from rotation, all sub-bands of a scale are combined and co-occurrence matrix of results is computed. Moreover, scale change in the image leads to the transfer of coefficients to other scales.

Therefore, to establish the independence of scale, we used those features extracted from a combination of sub-bands. The features were aggregated so that the overall vector consisted of 59 features (31 features related to the HMAX model descriptor and 28 features associated with GLCM descriptor). For this purpose, a series of

features from the combined matrix, coincidence matrix as well as the Gabor technique, which represents the description of the HMAX properties, is on a scale. We will calculate different values. Some of the features of the image are:

Contrast: it is obtained as,

$$Contrast = \sum_{g=0}^{G-1} g^2 \left(\sum_{g'=1}^{G-1} \sum_{g''=1}^{G-1} p(g', g'') \right) \quad (15)$$

$$|g' - g''| = g$$

Energy: it is measured in accordance,

$$Energy = \sum_{g=1}^G \sum_{g'=1}^G (p(g, g'))^2 \quad (16)$$

Entropy: This property is computed as,

$$Entropy = -\sum_{g=1}^G \sum_{g'=1}^G p(g, g') \log(p(g, g')) \quad (17)$$

Variance: or sum of squares,

$$Variance = \sum_{g=1}^G \sum_{g'=1}^G (g - \mu)^2 p(g, g') \quad (18)$$

Correlation: This criterion shows the linear dependence of the gray levels of the pixels that are located in the neighborhood and can be expressed as,

$$Correlation = \frac{1}{\sigma_x \sigma_y} \left(\sum_{g=1}^G \sum_{g'=1}^G (gg') p(g, g') - \mu_x \mu_y \right) \quad (19)$$

$P(i, j)$, the equivalence matrix of the (i, j) is normalized, and the denominator multiplied in the mean series is a deviation from the p_x and p_y criteria. $P_x(i)$ in the i -th diagram is a Co-occurrence of the summation of the matrix features.

In Eqs. (15)-(19), p is the image of the target area with dimension $G \times G$ pixels.

4.3. Performance Evaluation

4.3.1. Incorporation of All Features

Evaluation is conducted in two steps. The first step involves a performance evaluation of the method with many features and the second step includes few features. In both steps, factors of sensitivity, specificity and accuracy as well as K-fold evaluation were considered, in addition to the confusion matrix. Three factors of accuracy, sensitivity and specificity, which were proposed for measuring accuracy rate in detecting performance of the proposed system, are used according to Eqs. (20) - (22),

$$Accuracy = \left(\frac{N_{TP} + N_{TN}}{N_{TP} + N_{FN} + N_{TN} + N_{FP}} \right) \quad (20)$$

$$Sensitivity = \left(\frac{N_{TP}}{N_{TP} + N_{FN}} \right) \quad (21)$$

$$Specificity = \left(\frac{N_{TN}}{N_{TN} + N_{FP}} \right) \quad (22)$$

where N_{TP} is the number of positive corrects, N_{TN} is the number of negative correct, N_{FP} is the number of positive errors and N_{FN} is the number of negative errors in diagnosis of liver disease or cancer in sample CT images. The results of classification with maximum features (without feature selection) and aggregation of both descriptors in training and experiment stages are shown in Table 2.

4.3.2. Selected Features

In this step, the numbers of features are largely reduced to one third or a quarter of the total features.

For this purpose, 21 features were tested to evaluate their output. In Tables 4 and 5, the results of classification based on principal component analysis are presented for selecting the best features of algorithm. Moreover, the results of training and testing steps are depicted. In the presence of feature selection and inclusion of HMAX model (Table 4), the mean accuracy, specificity and sensitivity in training phase were equivalent to 0.9756, 0.9794 and 0.9573 respectively. Also, in the testing phase (Table 5) these were equivalent to 0.8503, 0.8133 and 0.8803 respectively, which indicated lower accuracy of the testing and higher accuracy of the training step.

Table 2. Assessment of algorithm in the second recognition step with maximum features and aggregation of both algorithms in the training stages.

Sens	Spec	Acc	FN	FP	TN	TP	K		
0.9705	0.9433	0.9586	2	3	50	66	1		
0.9852	0.9811	0.9834	1	1	52	67	2		
0.9710	0.9629	0.9674	2	2	52	66	3		
0.9705	0.9811	0.9752	2	1	52	66	4		
0.9411	0.9433	0.9421	4	3	50	64	5	K-fold Training Level	
0.8823	0.9245	0.9008	8	4	49	60	6		
1	1	1	0	0	53	68	7		
0.9855	0.9811	0.9836	1	1	52	68	8		
0.9705	0.9622	0.9669	2	2	51	66	9		
0.8997	0.8867	0.8925	7	6	47	61	10		
0.9573	0.9566	0.9570	29	23	508	652	-		Sum

Table 3. Assessment of algorithm in the second recognition step with maximum features and aggregation of both algorithms in the testing stages.

Sens	Spec	Acc	FN	FP	TN	TP	K		
0.7142	0.8333	0.7692	2	1	5	5	1		
1	0.8333	0.9285	0	1	5	6	2		
1	0.8000	0.9166	0	1	4	7	3		
0.8750	0.666	0.7857	1	2	4	7	4	K-fold Training Level	
0.8750	0.8333	0.8571	1	1	5	7	5		
0.8817	0.8332	0.8713	1	1	5	6	6		
0.7500	0.8333	0.7857	2	1	5	6	7		
0.8571	0.666	0.7692	1	2	4	6	8		
1	0.8333	0.9285	0	1	5	8	9		
0.8750	1	0.9285	1	0	6	7	10		
0.8803	0.8133	0.8503	9	11	48	65	-		Sum

Table 4. Evaluation of algorithm in the first recognition step with 21 features selected in the training steps.

Sens	Spec	Acc	FN	FP	TN	TP	K	
0.9421	0.9056	0.9262	4	5	48	65	1	
1	1	1	0	0	53	68	2	
0.9705	0.433	0.9586	2	3	50	66	3	
1	1	1	0	0	53	69	4	K-fold Training Level
1	1	1	0	0	53	68	5	
1	1	1	0	0	53	68	6	
0.9705	0.9433	0.9586	2	3	50	66	7	
0.9705	0.9433	0.9586	2	3	50	66	8	
0.9705	0.9811	0.9752	2	1	52	66	9	
0.9705	0.9811	0.9752	2	1	52	66	10	
0.9698	0.9794	0.9756	14	16	514	668	-	Sum

Table 5. Evaluation of algorithm in the first recognition step with 21 features selected in the testing steps.

Sens	Spec	Acc	FN	FP	TN	TP	K	
1	0.8333	0.9231	0	1	5	7	1	
1	1	1	0	0	6	8	2	
0.75	1	0.8571	2	0	6	6	3	
1	0.7248	0.8761	2	0	4	7	4	
0.8750	1	0.9258	1	0	6	7	5	K-fold Training Level
0.8817	0.8323	0.8713	1	1	5	6	6	
1	1	1	0	0	6	8	7	
1	0.7248	0.8761	1	0	4	7	8	
1	1	1	0	0	6	8	9	
1	0.8331	0.9231	0	1	5	7	10	
0.9037	0.9500	0.9170	8	3	53	71	-	Sum

5. CONCLUSION

The correct diagnosis of disease and liver cancers for a physician is not easy process. A physician will diagnose the condition by interpreting the results of one patient's experiments and comparing it with symptoms similar to other patients, or CT imaging or MRI in a person with a liver injury.

Regarding the nature of CT images, cancerous masses, liver lesions and different parts of the liver, in this paper, a method based on recognition of liver cancer is presented based on the use of intelligent processing technique.

Introducing the tools, it was initially suggested that CT images deprived of any possible liver damage from noise, and this could be done by applying a discrete wavelet transform. In the next step, the quality of the images was lost through the wavelet transform method of noise, and eventually the area in question was depicted in the image that was separated from other sections. In the next phase, we identified the pattern and based on the extraction of features, followed by the selection of the best features, the classification of the data, and thus the classification of the input images.

In the evaluation phase, factors such as accuracy, sensitivity, specificity and time were evaluated in the presence of an integrated learning algorithm. The emphasis was on correct data segmentation and K-fold (K=10) assessment method was used to test data in both training and testing stages. Optimized algorithms, particularly feature extraction algorithms with the lowest possible size (21 features out of 50 features) was adopted so that the classification system was able to predict the probability of liver disease with an accuracy of more than 91%. Prediction of these events can greatly reduce

lethal complications at different ages in a non-invasive manner. In future, we intend to increase recognition accuracy by reducing positive errors and delays in response. Also, it took few time in comparison with similar methods those the corresponding output is at a very good level and the proposed system can function as an integral independent part.

In this paper, the goal was to open the door to the new world of modern liver imaging technologies by using current smart systems and one of the major problems among patients who are left with liver cancer or cancer Grappling, or cancer detection.

REFERENCES

- [1] Stewart, B., & Wild, C. P. (2016). World cancer report 2014.
- [2] Rinella, M. E. (2015). Nonalcoholic fatty liver disease: a systematic review. *Jama*, 313(22), 2263-2273.
- [3] Siegel RL, Miller KD, Jemal A. Cancer statistics, 2016. *CA: a cancer journal for clinicians*. 2015 Jan 1;65(1):5-29.
- [4] Rahib L, Smith BD, Aizenberg R, Rosenzweig AB, Fleshman JM, Matrisian LM. Projecting cancer incidence and deaths to 2030: the unexpected burden of thyroid, liver, and pancreas cancers in the United States. *Cancer research*. 2014 Jun 1;74(11):2913-21.
- [5] Blachier, M., Leleu, H., Peck-Radosavljevic, M., Valla, D. C., & Roudot-Thoraval, F. (2013). The burden of liver disease in Europe: a review of available epidemiological data. *Journal of hepatology*, 58(3), 593-608.
- [6] Yoshimoto S, Loo TM, Atarashi K, Kanda H, Sato S, Oyadomari S, Iwakura Y, Oshima K, Morita H,

- Hattori M, Honda K. Obesity-induced gut microbial metabolite promotes liver cancer through senescence secretome. *Nature*. 2013 Jul 4;499(7456):97-101.
- [7] Vanni E, Bugianesi E. Obesity and liver cancer. *Clinics in liver disease*. 2014 Feb 28;18(1):191-203.
- [8] Livraghi T, Meloni F, Solbiati L, Zanusi G, Collaborative Italian Group using AMICA system. Complications of microwave ablation for liver tumors: results of a multicenter study. *Cardiovascular and interventional radiology*. 2012 Aug 1;35(4):868-74.
- [9] Sabih A, Sabih Q, Khan AN. Image perception and interpretation of abnormalities; can we believe our eyes? Can we do something about it? *Insights into imaging*. 2011 Feb 1;2(1):47-55.
- [10] Sabih A, Sabih Q, Khan AN. Image perception and interpretation of abnormalities; can we believe our eyes? Can we do something about it? *Insights into imaging*. 2011 Feb 1;2(1):47-55.
- [11] Lee, W. L., Chen, Y. C., & Hsieh, K. S. (2003). Ultrasonic liver tissues classification by fractal feature vector based on M-band wavelet transforms. *IEEE Transactions on Medical Imaging*, 22(3), 382-392.
- [12] Gletsos, M., Mougiakakou, S. G., Matsopoulos, G. K., Nikita, K. S., Nikita, A. S., & Kelekis, D. (2003). A computer-aided diagnostic system to characterize CT focal liver lesions: design and optimization of a neural network classifier. *IEEE transactions on information technology in biomedicine*, 7(3), 153-162.
- [13] Lim, S. J., Jeong, Y. Y., & Ho, Y. S. (2006). Automatic liver segmentation for volume measurement in CT Images. *Journal of Visual Communication and Image Representation*, 17(4), 860-875.
- [14] Mougiakakou, S. G., Valavanis, I. K., Nikita, A., & Nikita, K. S. (2007). Differential diagnosis of CT focal liver lesions using texture features, feature selection and ensemble driven classifiers. *Artificial Intelligence in Medicine*, 41(1), 25-37.
- [15] Okada, T., Shimada, R., Sato, Y., Hori, M., Yokota, K., Nakamoto, M., & Tamura, S. (2007, October). Automated segmentation of the liver from 3D CT images using probabilistic atlas and multi-level statistical shape model. In *International Conference on Medical Image Computing and Computer-Assisted Intervention* (pp. 86-93). Springer Berlin Heidelberg.
- [16] Heimann, T., Van Ginneken, B., Styner, M. A., Arzhaeva, Y., Aurich, V., Bauer, C., & Bello, F. (2009). Comparison and evaluation of methods for liver segmentation from CT datasets. *IEEE transactions on medical imaging*, 28(8), 1251-1265.
- [17] Militzer, A., Hager, T., Jager, F., Tietjen, C., & Hornegger, J. (2010, August). Automatic detection and segmentation of focal liver lesions in contrast enhanced CT images. In *Pattern Recognition (ICPR), 2010 20th International Conference on* (pp. 2524-2527).
- [18] Napel, S. A., Beaulieu, C. F., Rodriguez, C., Cui, J., Xu, J., Gupta, A., & Rubin, D. L. (2010). Automated retrieval of CT images of liver lesions on the basis of image similarity: method and preliminary results 1. *Radiology*, 256(1), 243-252.
- [19] Selver, M. A., Kocaoğlu, A., Demir, G. K., Doğan, H., Dicle, O., & Güzeliş, C. (2008). Patient oriented

- and robust automatic liver segmentation for pre-evaluation of liver transplantation. *Computers in Biology and Medicine*, 38(7), 765-784.
- [20] Quatrehomme, A., Millet, I., Hoa, D., Subsol, G., & Puech, W. (2012, October). Assessing the classification of liver focal lesions by using multi-phase computer tomography scans. In *MICCAI International Workshop on Medical Content-Based Retrieval for Clinical Decision Support* (pp. 80-91). Springer Berlin Heidelberg.
- [21] Zidan, A., Ghali, N. I., ella Hassamen, A., & Hefny, H. (2012, December). Level set-based CT liver image segmentation with watershed and artificial neural networks. In *Hybrid Intelligent Systems (HIS), 2012 12th International Conference on* (pp. 96-102).
- [22] Li, B. N., Chui, C. K., Chang, S., & Ong, S. H. (2012). A new unified level set method for semi-automatic liver tumor segmentation on contrast-enhanced CT images. *Expert Systems with Applications*, 39(10), 9661-9668.
- [23] Casciaro, S., Franchini, R., Massoptier, L., Casciaro, E., Conversano, F., Malvasi, A., & Lay-Ekuakille, A. (2012). Fully automatic segmentations of liver and hepatic tumors from 3-D computed tomography abdominal images: comparative evaluation of two automatic methods. *IEEE Sensors journal*, 12(3), 464-473.
- [24] Gunasundari, S., & Ananthi, M. S. (2012). Comparison and evaluation of methods for liver tumor classification from CT datasets. *International Journal of Computer Applications*, 39(18), 46-51.
- [25] Xu, J., Faruque, J., Beaulieu, C. F., Rubin, D., & Napel, S. (2012). A comprehensive descriptor of shape: method and application to content-based retrieval of similar appearing lesions in medical images. *Journal of digital imaging*, 25(1), 121-128.
- [26] Virmani, J., Kumar, V., Kalra, N., & Khandelwa, N. (2013). Pca-SVM based caD System for Focal liver lesions using B-mode ultrasound Images. *Defence Science Journal*, 63(5), 478.
- [27] Ji, H., He, J., Yang, X., Deklerck, R., & Cornelis, J. (2013). ACM-based automatic liver segmentation from 3-D CT images by combining multiple atlases and improved mean-shift techniques. *IEEE journal of biomedical and health informatics*, 17(3), 690-698.
- [28] Kumar, S. S., Moni, R. S., & Rajeesh, J. (2013). Automatic liver and lesion segmentation: a primary step in diagnosis of liver diseases. *Signal, Image and Video Processing*, 7(1), 163-172.
- [29] Öztürk, A. E., Ceylan, M., & Kıvrak, A. S. (2015). A new approach for liver classification using ridgelet/ripplelet-II transforms, feature groups and ANN. In *6th European Conference of the International Federation for Medical and Biological Engineering* (pp. 130-133). Springer International Publishing.
- [30] Balagurunathan, Y., Gu, Y., Wang, H., Kumar, V., Grove, O., Hawkins, S., & Gillies, R. J. (2014). Reproducibility and prognosis of quantitative features extracted from CT images. *Translational oncology*, 7(1), 72-87.
- [31] Singh, M., Singh, S., & Gupta, S. (2014). An information fusion based method for liver classification using texture analysis of ultrasound images. *Information Fusion*, 19, 91-96.

- [32] Tomoshige, S., Oost, E., Shimizu, A., Watanabe, H., & Nawano, S. (2014). A conditional statistical shape model with integrated error estimation of the conditions; application to liver segmentation in non-contrast CT images. *Medical image analysis*, 18(1), 130-143.
- [33] Hirata, K., Kobayashi, K., Wong, K. P., Manabe, O., Surmak, A., Tamaki, N., & Huang, S. C. (2014). A semi-automated technique determining the liver standardized uptake value reference for tumor delineation in FDG PET-CT. *PloS one*, 9(8), e105682.
- [34] Mala, K., Sadasivam, V., & Alagappan, S. (2015). Neural network based texture analysis of CT images for fatty and cirrhosis liver classification. *Applied Soft Computing*, 32, 80-86.
- [35] Roth, H. R., Farag, A., Lu, L., Turkbey, E. B., & Summers, R. M. (2015, March). Deep convolutional networks for pancreas segmentation in CT imaging. In *SPIE Medical Imaging* (pp. 94131G-94131G). International Society for Optics and Photonics.
- [36] Conze, P. H., Rousseau, F., Noblet, V., Heitz, F., Memeo, R., & Pessaux, P. (2015, October). Semi-automatic liver tumor segmentation in dynamic contrast-enhanced CT scans using random forests and supervoxels. In *International Workshop on Machine Learning in Medical Imaging* (pp. 212-219). Springer International Publishing.
- [37] Mostafa, A., Elfattah, M. A., Fouad, A., Hassanien, A. E., & Hefny, H. (2016). Enhanced Region Growing Segmentation for CT Liver Images. In *The 1st International Conference on Advanced Intelligent System and Informatics (AISII2015)*, November 28-30, 2015, Beni Suef, Egypt (pp. 115-127). Springer International Publishing.
- [38] Sonka, M., Hlavac, V., & Boyle, R. (2014). *Image processing, analysis, and machine vision*. Cengage Learning.
- [39] Yan, R., Shao, L., & Liu, Y. (2013). Nonlocal hierarchical dictionary learning using wavelets for image denoising. *IEEE Transactions on Image Processing*, 22(12), 4689-4698.
- [40] Samson, C., & Sastry, V. U. K. (2012). Novel image encryptions supported by compression using multilevel wavelet transform. *IJACSA) International Journal of Advanced Computer Science and Applications*, 3(9).
- [41] Kim, J. W., Song, J., Lee, S., & Park, I. C. (2007, May). Tiled interleaving for multi-level 2-D discrete wavelet transform. In *2007 IEEE International Symposium on Circuits and Systems* (pp. 3984-3987).
- [42] Hamed, I., & Owis, M. I. (2016). Automatic Arrhythmia Detection Using Support Vector Machine Based on Discrete Wavelet Transform. *Journal of Medical Imaging and Health Informatics*, 6(1), 204-209.
- [43] Haralick, R. M., & Shanmugam, K. (1973). Textural features for image classification. *IEEE Transactions on systems, man, and cybernetics*, (6), 610-621.
- [44] Weszka, J. S., Dyer, C. R., & Rosenfeld, A. (1976). A comparative study of texture measures for terrain classification. *IEEE Transactions on Systems, Man, and Cybernetics*, 4(SMC-6), 269-285.103.
- [45] Mallat, S. G. (1989). A theory for multiresolution signal decomposition: the wavelet representation. *IEEE*

- transactions on pattern analysis and machine intelligence, 11(7), 674-693.
- [46] Huang, D., Zhang, K., & Zhang, D. (2015, June). Improvement on Gabor Texture Feature Based Biometric Analysis Using Image Blurring. In International Conference on Intelligent Science and Big Data Engineering (pp. 420-430). Springer International Publishing.
- [47] Shen, L., & Yin, Q. (2009, August). Texture classification using curvelet transform. In Proceedings of the International Symposium on Information Processing (ISIP'09) (pp. 319-324).
- [48] Hubel, D. H., & Wiesel, T. N. (1959). Receptive fields of single neurones in the cat's striate cortex. *The Journal of physiology*, 148(3), 574-591.
- [49] Hubel, D. H., & Wiesel, T. N. (1962). Receptive fields, binocular interaction and functional architecture in the cat's visual cortex. *The Journal of physiology*, 160(1), 106-154.
- [50] Serre, T. , Kouh, M., Cadieu, C., Knoblich, U., Kreiman, G., & Poggio, T. (2005). A theory of object recognition: computations and circuits in the feedforward path of the ventral stream in primate visual cortex, AI Memo 2005-036/CBCL Memo 259, MIT, Cambridge, MA.
- [51] Meyer, D., & Wien, F. T. (2015). Support vector machines. The Interface to libsvm in package e1071.